Innovative data weighting for iterative reconstruction in a helical CT security baggage scanner

Sherman J. Kisner
Pengchong Jin
Charles A. Bouman
Electrical and Computer Engineering
Purdue University
West Lafayette, Indiana
Email: {kisner, jin36, bouman}
@purdue.edu

Ken Sauer
Department of Electrical Engineering
University of Notre Dame
South Bend, Indiana
Email: sauer@nd.edu

Walter Garms
Todd Gable
Seungseok Oh
Matthew Merzbacher
Sondre Skatter
Morpho Detection, Inc.
Newark, California
Email:{wgarms,tgable,soh,mmerz,sskatter}
@morphodetection.com

***Abstract*—X-ray computed tomography (CT) currently has widespread application in air travel security systems for the purpose of baggage screening. This work presents an implementation of a fully 3D model-based iterative reconstruction (MBIR) algorithm mapped to a multi-slice helical CT security scanner. We introduce innovations in the data model that are designed to enhance image quality for typical scenes encountered in the security setting. In particular, we explore alternatives in the weighting of the measurements in order to more accurately reconstruct uniform regions and suppress metal artifacts. We compare images from the model-based approach to direct analytical reconstructions, indicating that the MBIR produces higher resolution and lower-noise reconstructions with suppressed metal streaking. The image improvements afforded by MBIR can provide for better operator experience and potentially enable enhanced performance of automatic threat detection (ATD).**

I. Introduction

X-ray computed tomography (CT) has become an integral component of air travel security systems for clearing containers placed in the hold of commercial aircraft. These CT systems are tasked with producing a three dimensional image (or a series of 2D images) of the contents of a suitcase or cargo container that is suitable for both visual inspection and for analysis by automatic threat detection (ATD) algorithms. The quality of the CT images is a key factor in the performance of a screening system because any container that cannot be cleared from the images alone must undergo additional screening which requires significantly more time and resources.

CT image quality is governed not only by the engineering of the physical system itself, but also by the image reconstruction methods employed which transform the raw X-ray projection measurements into meaningful images [1], [2]. Generally speaking, the choice of the reconstruction approach involves a trade-off between the resilience to image noise and distortion, and the time and computing power required to perform the reconstruction. Direct analytical reconstruction such as *filtered back-projection* (FBP) and the *direct Fourier method* (DFM) have remained attractive due to their relatively light computational burden, as well as their long history of use in medical CT. However, deviations from the theoretical forward projection model are in many cases not easily overcome, and can result in significant image distortion. Dense materials such as metal, for example, can be particularly problematic in this respect; and while it is rarely encountered in significant quantities in medical scans, metal is usually found to some extent in nearly all checked luggage.

Model-based iterative reconstruction (MBIR) is a framework that incorporates detailed scanner geometry and measurement noise characteristics along with a statistical model for the image itself, combined into a single cost optimization problem [3], [4]. This framework allows a great deal of flexibility to tune the algorithm to a particular scanner and application. Recent investigations studied the implementation of MBIR in security CT systems having a limited-view geometry [5], and a helical scan geometry [6]. For multi-slice helical scan CT in particular, modeling the 3D geometry explicitly accounts for the trajectory of the X-ray source, the cone angle of the detector array, and the detector point-spread function. The model also accounts for measurement degradation due to photon quantum noise and electronic noise in the detectors. Incorporating this information directly into the reconstruction allows less reliance on pre-correction and reformatting (interpolation) of the data to a standard set of tomographic measurements, which is required for most direct reconstruction methods.

This work presents an implementation of fully 3D MBIR reconstruction for a multi-slice helical CT system designed for security screening. We introduce innovations to the MBIR model to enhance image quality specifically for the security application. We first demonstrate that the traditional MBIR noise weighting can substantially reduce metal artifacts, but under certain conditions can also contribute to irregular textures in uniform materials. We then introduce a novel weighting function that adaptively combines the traditional weights with a power-law scaling, resulting in reconstructions with greatly improved texture and reduced metal streaking. We also show substantial improvements afforded by detector afterglow correction [7] and calibration for fan beam offset.

For assessment we compare the MBIR reconstructions to the resident DFM based reconstructions employed in the system. The MBIR results with the adapted noise weighting demonstrate higher resolution and lower noise images, with greater suppression of metal-induced artifacts.

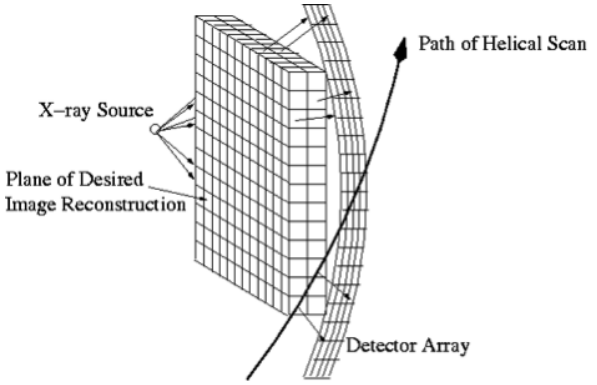

Fig. 1. Illustration of the key components of a multi-slice helical scan CT system. The X-ray source and detector array are affixed to a rotating gantry, and the scan target is translated through the plane of rotation as measurements are sampled from the array. As indicated here, it is usually convenient to consider the target as fixed and the gantry as translating past the imaging volume.

II. Background

A. Multi-slice Helical Scan CT

The CT system of interest in this study is a third generation CT scanner in which the X-ray source and detectors rotate about a fixed axis, and the target objects are continuously fed through on a conveyer belt. It is common to define a coordinate system as fixed with respect to the image volume, with the source and detectors translating to produce a helical trajectory, as illustrated in Fig. 1. A multi-slice system has a detector array consisting of many rows (slices) and typically hundreds of columns of detector cells arranged in an arc, providing a sufficient number of projections to recover a 3D image of the scan target.

Our data model assumes a linear forward projection in which the object density image, $x \in \mathbb{R}^M$, and the projections, $y \in \mathbb{R}^N$, in the absence of noise are related by a sparse matrix operator A,

$$y = Ax \ . \tag{1}$$

The matrix coefficient A_{ij} represents the contribution of voxel j in forming projection i. In our case the elements of A are calculated using a distance-driven projector [3], [8].

B. Model-Based Iterative Reconstruction

In the MBIR framework, we consider the image, x, and the projection measurements, y, as random vectors, and the reconstructed image is computed as the maximum *a posteriori* (MAP) estimate,

$$\hat{x} = \underset{x \geq 0}{\text{argmin}} \{ -\log p(y|x) - \log p(x) \} \ . \tag{2}$$

The likelihood function $p(y|x)$ contains the characterization of the measurement data, including the projection model and measurement noise. The prior distribution, $p(x)$, of the image plays the important role of regularizing the solution, which mitigates the effects of having a data set that is noisy, incomplete, or that contains aberrations from the assumed data model.

The measured photon count, λ_i, corresponding to projection i can be modeled as Poisson with mean $\bar{\lambda}_i = \bar{\lambda}_{T,i} e^{-A_{i*}x}$, where $\bar{\lambda}_{T,i}$ is the input photon rate for projection i, and A_{i*} denotes the i^{th} row of the projection matrix. From the Poisson model, a second-order Taylor expansion can be used to approximate the log likelihood term by the following [9],

$$\log p(y|x) \approx -\frac{1}{2}(y - Ax)^T D(y - Ax) + g(y) \tag{3}$$

where D is a diagonal weighting matrix with entries $D_{ii} = \lambda_i$, and $g(y)$ combines terms that are constant with respect to x. Note in this form, the photon count, λ_i, acts as a weighting coefficient for the cost term, $(y_i - A_{i*}x)^2$, associated with projection i. This has a simple intuition in that smaller photon counts are less reliable measurements, and hence are weighted less in the cost function. An advancement of this result is the weighting $D_{ii} = \lambda_i^2/(\lambda_i + \sigma_i^2)$, which accounts for both photon statistics and additive electronic measurement noise [4].

A common class of priors in imaging is a Markov random field (MRF), which can be specified entirely through local pixel interactions. In the current study we consider only pairwise interactions, and so the prior is defined by a Gibbs distribution of the following form,

$$p(x) = \frac{1}{z} \exp \left\{ - \sum_{\{s,r\} \in \mathcal{C}} b_{s,r} \rho(x_s - x_r) \right\} \tag{4}$$

where $\rho(\cdot)$ is a positive and symmetric *potential function*, $\mathcal{C}$ is the set of all pairwise cliques defined by the neighborhood system, and z is a normalizing constant. For the 3D reconstructions in this study, the cliques are formed from a 26-point neighborhood which comes from the nearest neighbors surrounding a given pixel in all 3 dimensions. Also, in this study we utilize an absolute value prior, $\rho(\Delta) = |\Delta|$, which is closely related to *total variation* (TV) regularizer [10], often used in imaging problems.

Combining, the reconstruction is obtained by solving the following optimization,

$$\hat{x} = \underset{x \geq 0}{\text{argmin}} \left\{ \frac{1}{2} \|y - Ax\|_D^2 \ + \sum_{\{s,r\} \in \mathcal{C}} b_{s,r} \rho(x_s - x_r) \right\} \ . \tag{5}$$

Here we compute the solution, $\hat{x}$, with a parallelized implementation of iterative coordinate descent (ICD) which solves the global optimization by a series of 1D minimizations with respect to each voxel [6], [9].

III. Methods and Results

A. Preliminary Model Corrections

We first briefly note two model corrections that were strongly beneficial for all of the reconstructions presented in this study.

1) Detector Afterglow: X-ray scintillation detectors exhibit an *afterglow* property, which is a temporally smoothed response due to physical properties of the scintillation crystal. We corrected for detector afterglow using a recursive filter described in [7] on the raw scanner measurements. Figure 2 illustrates the effect of afterglow correction on MBIR reconstructions. The example shows an axial slice with significantly improved resolution as a result of the correction.

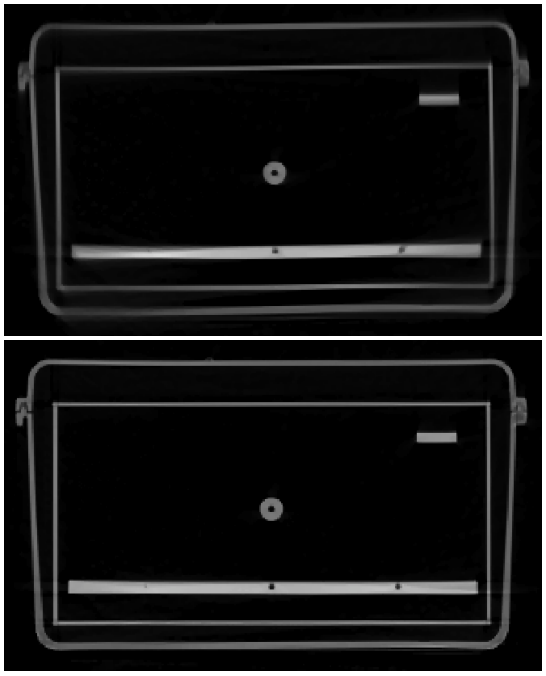

Fig. 2. Illustration of the effect of afterglow correction. MBIR reconstructions on (a) raw, and (b) afterglow corrected measurements.

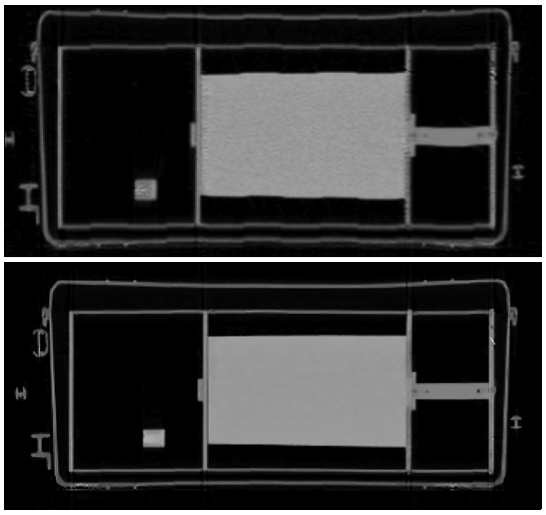

Fig. 3. Accounting for a small displacement in the relative mounting position of the detector array. (a) Original DFM reconstruction, (b) MBIR accounting for a fan angle offset. The horizontal axis is in the z-direction (perpendicular to the plane of gantry rotation).

2) Fan Angle Offset: Image reconstruction algorithms inherently assume an exact geometry of the system. A slight displacement in the mounting position of the detector array relative to the source, even within manufacturing tolerances, was found to produce a clear periodic displacement artifact in the reconstructed target. Figures 3(a) and 3(b) illustrate the effect of accounting for a small offset in the fan angle of the detector array.

B. Data Weighting Matrix

From the form of the likelihood in Eq. (3), the diagonal entries D_{ii} take the role of the approximate inverse variance of the projections y_i. This is true for $D_{ii} = \lambda_i$ when considering photon noise alone, and is the principle behind the result $D_{ii} = \lambda_i^2/(\lambda_i + \sigma_i^2)$ accounting for both photon and electronic noise. The inverse variance is a logical choice for the weighting of the sinogram entries, y_i, in contributing to the solution of (5). However there is motivation for further exploration of these weights. For one, that D_{ii} represents an inverse variance presupposes that the projection y_i varies about a mean $A_{i*}x$. Inaccuracy in the linearized and discretized projection model, as well as other biasing influences (e.g. beam-hardening, non-linear partial volume effects, scatter) can also affect the reliability of each data term in forming the solution.

Experimentally, we found an advantage in generalizing the weighting D_{ii} as a function of the counts $f(\lambda_i)$. One in particular is the family of power law functions of the form

$$D_{ii} = (\lambda_i/\lambda_{T,i})^r \tag{6}$$

where λ_i is the target scan count, $\lambda_{T,i}$ is the air scan count (a separate scan with no target present), and $0 \leq r \leq 1$. The case $r = 1$ is equivalent to the original Poisson-induced weighting, and the effect of decreasing r from 1 is primarily to increase the relative weights of the lower-count measurements.

Figures 4(a) and 4(b) show a slice from a DFM reconstruction and an MBIR reconstruction, using $D_{ii} = \lambda_i$ and $\rho(\cdot) = |\cdot|$, of a large uniform-density cylinder. The irregular texture in the MBIR result is a behavior we often observe when using the traditional weightings in reconstructing relatively large objects that produce highly attenuated X-ray measurements. Figure 4(c) shows the effect of reducing r to 0.5, resulting in a substantial improvement in the variance and texture within the uniform object.

A negative side-effect of increasing the relative weights of the lower-count measurements is to also exacerbate distortion due to highly dense materials such as metal. This effect is illustrated in Figure 5(b) and 5(c) for reconstructions of a smaller cylinder containing tungsten pins. Note the non-uniform texture for $r = 1$ is not as apparent compared to the result in Figure 4(b) due the cylinder's smaller size.

To retain both improvement in bulk object reconstruction and resilience to metal artifacts, we produced a mixture of these weightings that depends on the detected presence of metal. To this end, we first define a function I_i indicating the likely presence of metal along projection ray i.

$$I_i = \begin{cases} 1 & , \text{ if for some } j, \text{ both } A_{ij} > 0 \text{ and } x_j^{(0)} > T \\ 0 & , \text{ otherwise} \end{cases} \tag{7}$$

Here $x_j^{(0)}$ is the CT number for voxel j from an initial reconstruction, and T is a threshold CT value for metal. The weights are then mixed according to

$$D_{ii} = I_i\,(\lambda_i/\lambda_{T,i}) + (1 - I_i)\,(\lambda_i/\lambda_{T,i})^{0.5} \tag{8}$$

which selects $r = 1$ or $r = 0.5$ for a given projection ray depending on the simple metal indicator. Figures 4(d) and 5(d) show the corresponding results using the mixed weighting. In this study we use $T = 3000$ Hounsfield units (HU) (offset so that air=0 HU, water=1000 HU).

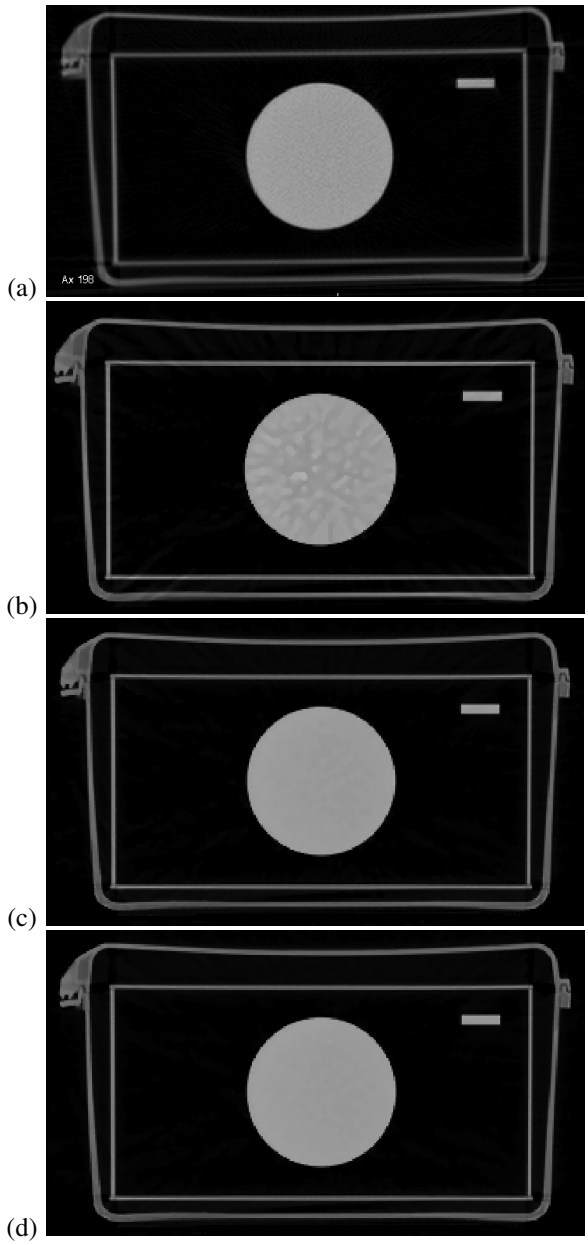

Fig. 4. Effect of power law weighting in the data matrix entries. Target is a large uniform-density acetal cylinder (diam=15cm). (a) DFM; (b) MBIR, r=1; (c) MBIR, r=1/2; (d) MBIR, r=$\{1,1/2\}$ mixture.

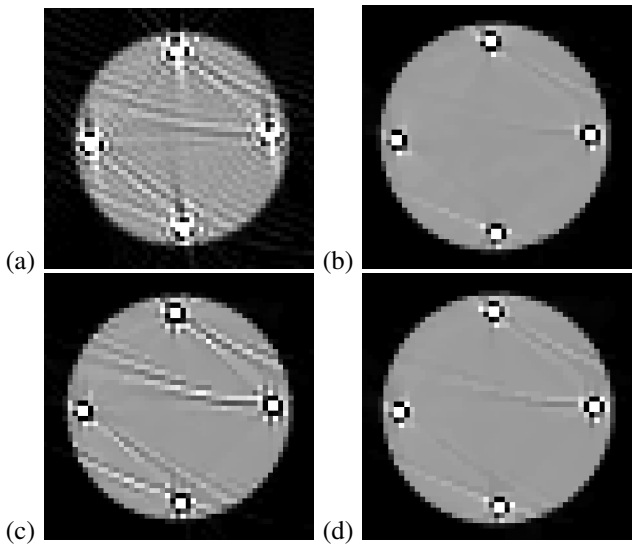

Fig. 5. Effect of power law weighting in the data matrix entries. Target is a uniform-density acetal cylinder (diam=8cm) containing tungsten pins. (a) DFM; (b) MBIR, r=1; (c) MBIR, r=1/2; (d) MBIR, r=$\{1,1/2\}$ mixture.

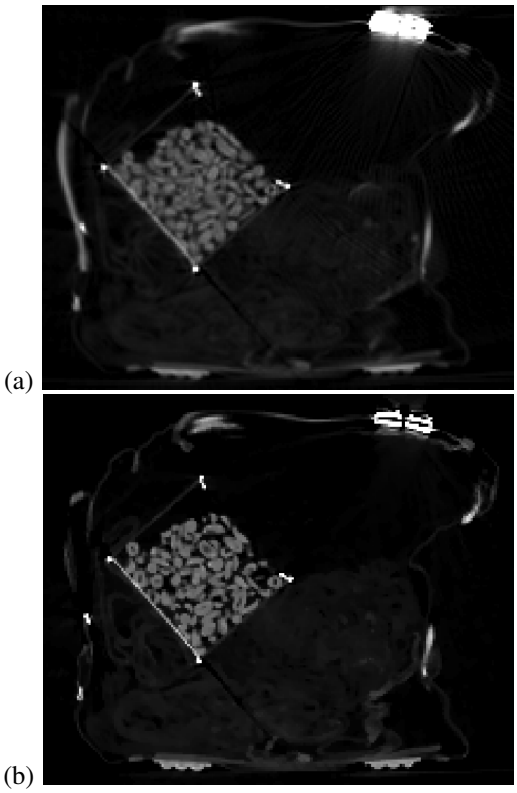

Fig. 6. Comparison of (a) DFM, and (b) MBIR reconstructions for a bag containing clothing and snacks.

C. Comparison of MBIR and DFM Reconstructions

For further evaluation, model-based reconstructions were computed for several luggage scans using the new data weighting in Eq. (8), Figures 6, 7, 8, and 9 present select regions from these results alongside DFM reconstructions for comparison. Afterglow correction was performed on these scans prior to both MBIR and DFM reconstruction. Figures 7 and 8 demonstrate a dramatic reduction in metal-induced streaking while reproducing uniform materials with little noise. Figures 6 and 9 highlight improvements with respect to resolution and object discrimination.

These image improvements afforded by MBIR provide for both better operator experience and enhanced performance of automatic threat detection (ATD). Operator experience is beyond the scope of this paper, but it is evident that a cleaner image will help operators with the fast and effective clearing of benign luggage.

We evaluated the qualitative impact of the improved image reconstructions on Morpho Detection's proprietary ATD algorithms. The cleaner objects in Figure 6 can improve segmen-

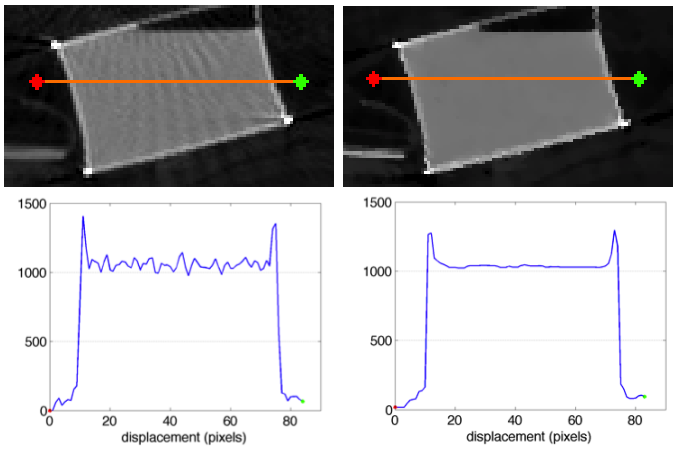

(a) DFM (b) MBIR

Fig. 7. Comparison of DFM and MBIR reconstructions on a baggage scan. The region highlights a bulk uniform material susceptible to distortion from a nearby object.

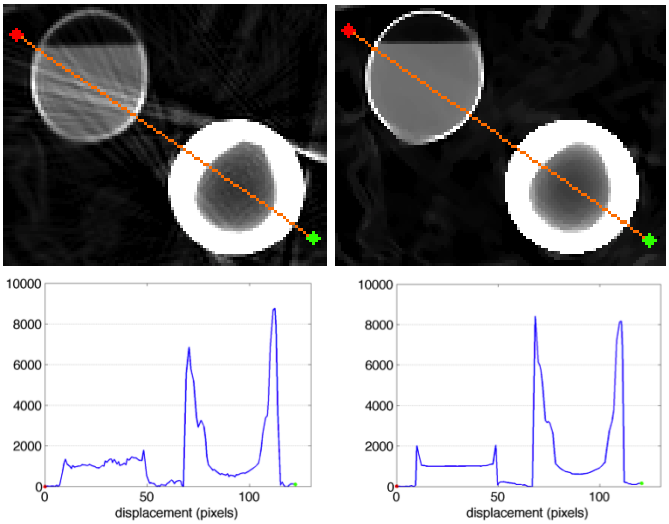

(a) DFM (b) MBIR

Fig. 8. Comparison of DFM and MBIR reconstructions on a baggage scan. The region highlights a bulk uniform material susceptible to distortion from a nearby object.

tation, leading to better object identification (and consequent classification). Noise reduction (Figures 7 and 8) also helps with classification, as well as with distinguishing containers from their contents. Figure 9 shows how MBIR could allow ATD to separate adjoining objects for further analysis. Each image improvement leads to a reduction in false alarms due to incorrect segmentation, processing, or classification. In turn, the reduction in false alarms opens an opportunity for increased detection on challenging configurations or new threats.

IV. Conclusion

This work presented an implementation of fully 3D MBIR reconstruction for a multi-slice helical CT scanner used for security screening. We introduced a novel data weighting in the MBIR model to enhance image quality for security applications. In comparing to DFM, the MBIR reconstructions demonstrated substantial improvement in resolution, noise

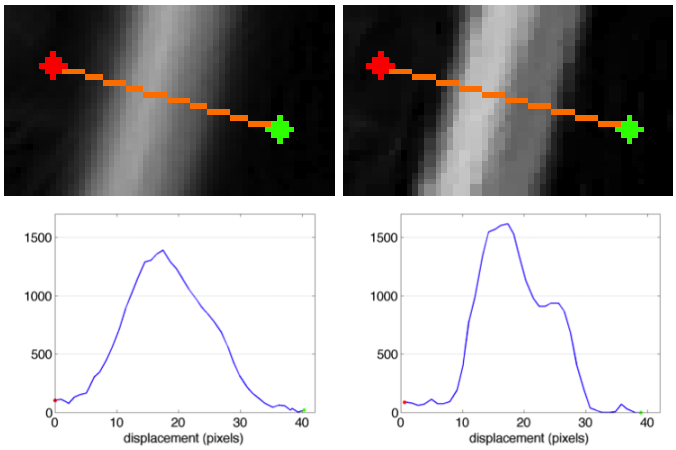

(a) DFM (b) MBIR

Fig. 9. Comparison of DFM and MBIR reconstructions on a baggage scan. The region highlights the discrimination between two adjacent objects.

reduction, and reduction of metal-induced streaking. These image improvements can be used to reduce false alarms in existing ATD algorithms or to reduce the cost of new detection schemes.

Acknowledgment

This work was supported by the U.S. Department of Homeland Security under Award Number 2008-ST-061-ED0001.

References

[1] T. Buzug, *Computed Tomography: From Photon Statistics to Modern Cone-Beam CT*. Berlin: Springer, 2008.

[2] J. Hsieh, *Computed Tomography: principles, design, artifacts, and recent advances*, 2nd ed. Bellingham, WA: SPIE, 2009.

[3] J.-B. Thibault, K. Sauer, C. Bouman, and J. Hsieh, "A three-dimensional statistical approach to improved image quality for multi-slice helical CT," *Medical Physics*, vol. 34, no. 11, pp. 4526–4544, 2007.

[4] J.-B. Thibault, C. A. Bouman, K. D. Sauer, and J. Hsieh, "A recursive filter for noise reduction in statistical iterative tomographic imaging," in *Proc. SPIE 6065, Computational Imaging IV*, Jan. 2006.

[5] S. J. Kisner, E. Haneda, C. A. Bouman, S. Skatter, M. Kourinny, and S. Bedford, "Limited view angle iterative CT reconstruction," in *Proc. SPIE 8296, Computational Imaging X*, Feb. 2012.

[6] P. Jin, E. Haneda, K. D. Sauer, and C. A. Bouman, "A model-based 3D multi-slice helical CT reconstruction algorithm for transportation security application," in *Proc. of The 2nd International Conference on Image Formation in X-Ray Computed Tomography*, June 2012.

[7] J. Hsieh, O. E. Gurmen, and K. F. King, "A recursive correction algorithm for detector decay characteristics in CT," in *Proc. SPIE, Medical Imaging 2000: Phyics of Medical Imaging*, vol. 3977, 2000, pp. 298–305.

[8] B. De Man and S. Basu, "Distance-driven projection and backprojection in three dimensions," *Physics in Medicine and Biology*, vol. 49, no. 11, pp. 2463–2475, 2004.

[9] K. Sauer and C. Bouman, "A local update strategy for iterative reconstruction from projections," *IEEE Trans. on Signal Processing*, vol. 41, no. 2, pp. 534–548, 1993.

[10] L. I. Rudin, S. Osher, and E. Fatemi, "Nonlinear total variation based noise removal algorithms," *Physica D: Nonlinear Phenomena*, vol. 60, no. 14, pp. 259 – 268, 1992.